

Data-Driven Optical to Thermal Inference in Pool Boiling Using Generative Adversarial Networks

Qianxi Fu¹, Youngjoon Suh¹, Xiaojing Zhang¹, Yoonjin Won^{1,2,*}

¹Department of Mechanical and Aerospace Engineering, University of California, Irvine, Irvine, CA 92697, USA

²Department of Electrical Engineering and Computer Science, University of California, Irvine, Irvine, CA 92697, USA

*Corresponding Authors Email: won@uci.edu

Abstract

Phase change plays a critical role in thermal management systems, yet quantitative characterization of multiphase heat transfer remains limited by the challenges of measuring temperature fields in chaotic, rapidly evolving flow regimes. While computational methods offer spatiotemporal resolution in idealized cases, replicating complex experimental conditions remains prohibitively difficult. Here, we present a data-driven framework that leverages a conditional generative adversarial network (CGAN) to infer temperature fields from geometric phase contours in a canonical pool boiling configuration where advanced data collection techniques are restricted. Using high-speed imaging data and simulation-informed training, our model demonstrates the ability to reconstruct temperature fields with errors below 6%. We further show that standard data augmentation strategies are effective in enhancing both accuracy and physical plausibility of the predicted maps across both simulation and experimental datasets when precise physical constraints are not applicable. Our results highlight the potential of deep generative models to bridge the gap between observable multiphase phenomena and underlying thermal transport, offering a powerful approach to augment and interpret experimental measurements in complex two-phase systems.

Keywords: Pool boiling, deep learning, phase change, multiphase, generative neural networks

1. Introduction

Pool boiling plays a vital role in thermal management systems across a wide spectrum of technologies, from industrial power generation [1] to electronics cooling [2]. Gaining a detailed understanding of the underlying thermal transport processes is essential for optimizing performance and ensuring reliability. A central challenge in advancing the science of boiling lies in the difficulty of capturing key thermal fields, particularly temperature, with sufficient spatial and temporal resolution. Although engineering design has traditionally relied on empirical correlations and theoretical models informed by experimental observations, these approaches depend on measurable quantities that remain elusive in complex, multiphase environments. Unlike single-phase systems, pool boiling involves rapid phase transitions, interfacial instabilities, and transient bubble dynamics that render conventional measurements difficult to obtain [3]. Consequently, the absence of high-resolution thermal field data continues to hinder our ability to obtain deeper physical insight and the development of more predictive modeling frameworks.

To address the difficulty of capturing thermal field data in pool boiling, various experimental diagnostics have been developed to extract localized or indirect measurements of heat transfer. Microheater arrays with integrated heat flux sensors, for example, allow pointwise estimation of thermal transport near nucleation sites, offering insight into microlayer evaporation and surface convection [4]. High-speed imaging enables visualization of vapor dynamics and bubble interactions, which can help infer heat transfer modes [5]. Infrared thermography, when synchronized with visual imaging, has further enhanced our ability to track surface temperature variations over time [6]. More recent advanced techniques such as planar laser induced fluorescence (PLIF) have been developed to directly measure the temperature distribution within multiphase structures such as droplets [7], liquid films [8,9] and spray mixture [10]. While each of these methods has yielded valuable observations, they remain constrained by the complex and delicate experimental setup required to achieve high spatial and temporal resolution [3]. Most importantly, they do not provide dense, field-level thermal data in a form suitable for generalized modeling or data-driven learning. These limitations motivate the search for alternative approaches capable of extracting richer thermal information from accessible measurements.

Given the challenges of acquiring comprehensive thermal data experimentally, simulations have been used to gain insight into boiling heat transfer by resolving fluid and thermal fields under controlled conditions. Computational fluid dynamics (CFD), including methods such as volume-of-fluid, level set, and front-tracking [11], has enabled detailed studies from single-bubble growth to complex bubble interactions [12-14]. The lattice Boltzmann method (LBM) in particular has gained attention for its ability to simulate complex interfacial phenomena without explicit interface tracking [15,16]. Furthermore, the mesoscopic nature of LBM makes it a balanced CFD method both in terms of accuracy and computational speed. While these techniques have demonstrated qualitative and even quantitative agreement with certain experimental results, they remain limited in their broader applicability. Accurately capturing multiphase dynamics requires careful modeling of interfacial motion, latent heat transfer, and variable material properties, which are all highly sensitive to numerical resolution and boundary conditions. Moreover, boiling spans a wide range of spatial and temporal scales that are difficult to capture within a single computational framework. High-fidelity simulations often suffer from high computational cost, limited convergence, and difficulty in handling realistic geometry or material variability [10]. These challenges restrict the ability of traditional CFD methods to provide generalizable, high-throughput predictions for real-world boiling systems.

Deep learning has emerged as a powerful tool for modeling complex physical systems that are difficult to describe analytically or simulate with high fidelity. Its generalizability and efficiency have delivered promising results as more research is devoted to the application of deep learning in a variety of multiphase systems [17]. In particular, deep learning-assisted computer vision models have shown to be capable of automating data collection tasks such as bubble detection and phase segmentation [18-26], greatly reducing manual effort in analyzing visual datasets. This allows the access to additional structural and statistical data that is previously difficult to obtain. Moreover, it has enabled effective training of neural networks on large datasets to predict quantities such as heat transfer coefficients [21,23,26] and perform flow regime classification [18,20,23,24]. In parallel, physics-informed neural networks (PINNs) have shown promise as surrogate models by embedding governing equations into the learning process, offering improved physical consistency in the absence of dense data [27]. However, PINNs often require known boundary and initial conditions which may not be available, and can struggle with convergence or accuracy in chaotic, data-sparse multiphase systems [28,29]. In contrast, generative deep learning models such as generative adversarial networks (GANs) [30] excel at learning mappings directly from data that can possess complex features, without requiring explicit knowledge of the underlying physics and patterns. GANs and their variants have shown to be effective in

tasks such as image-to-image translation [31] and high-resolution image generation [32,33]. In the realm of heat transfer and fluid dynamics, GANs have been readily employed in generating high-resolution 3D chaotic turbulent flow [34] and temperature data inference in single-phase system [35]. Furthermore, recent works such as inference on electromagnetic properties in three-phase flow [36] and flow rate prediction in gas-liquid mixture [37] have motivated investigation of the applicability of generative neural networks in multiphase systems.

In this work, we present a deep learning framework for predicting side temperature fields in pool boiling systems using only easily measurable data including visual information of the phase geometry and pointwise temperature measurements. To train the model, we generate paired temperature and phase contour data, which serves as the only viable ground truth for supervised learning, using a hybrid lattice Boltzmann and finite difference (LB-FD) method [38] that capitalizes on the inherent efficiency of the simulation method. A conditional generative adversarial network (CGAN) [39] is used to learn the mapping between liquid–vapor interface geometry and the underlying temperature distribution. Once trained, the model is applied directly to experimental data through extracted phase contours from high-speed imaging, enabling temperature field prediction without the need for intrusive measurements. This approach represents a step forward in bridging simulation-based learning with experimental analysis, allowing us to infer otherwise inaccessible thermal information from readily obtainable visual data. We further apply data augmentation techniques to improve prediction robustness and physical consistency. This paper details the model architecture, training process, and evaluation results, and explores the broader implications of applying deep generative models to multiphase heat transfer problems.

2. Framework

We develop a deep learning framework to infer temperature fields in pool boiling systems using only high-speed visual data and limited thermal measurements following a general approach outlined in Fig. 1. We train a base CGAN model [39] on data generated from a LB–FD simulation method [38], which provides paired temperature and phase contour fields that serve as ground truth. To enable application to experimental observations, we preprocess both simulation and experimental data into a shared input format consisting of a phase contour map, denoted by ϕ ; and an initial temperature map, denoted by T_0 prior to training. For simulation data, we derive the phase contour by thresholding the density field to distinguish solid, liquid, and vapor regions. We select the initial temperature frame after thermal conduction through the solid layer stabilizes, so that the model focuses on meaningful temperature evolution within the liquid and vapor phases.

After training, we apply the model to a canonical pool boiling experiment as shown in Fig. 2(a), where the only available measurements are two-dimensional high-speed video and pointwise thermocouple readings at the heater surface. We do not use advanced diagnostics such as infrared thermography or particle-based flow visualization, reflecting the limitations commonly encountered in practical experiments. We process experimental data into the same input structure as the simulation data: we extract phase contours from high-speed images by instance segmentation using a pre-trained Mask R-CNN [23,40] and manually construct the initial temperature field from thermocouple measurements. This consistent data formatting bridges experimental and simulation data, using the bubble masks to infer critical thermal-fluid properties in the surrounding regions, providing a novel pathway for analyzing bubble dynamics and their impact on the liquid environment.

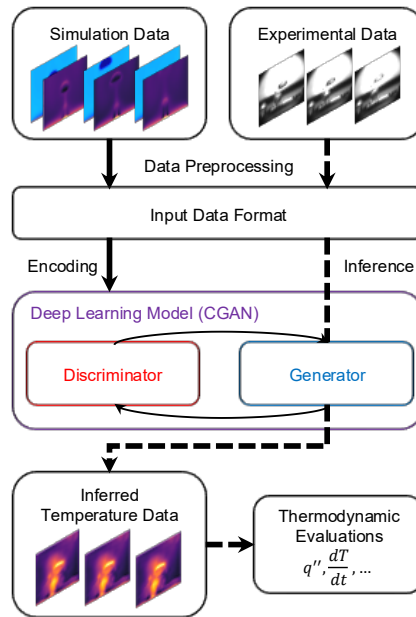


Fig. 1. General approach to generating additional data from available experimental data. Deep learning model (CGAN) encodes simulation data through model training (solid arrow path). After training, the generator component of CGAN makes the inference from experimental data, which enables additional analysis and evaluation (dashed arrow path).

3. Methods

3.1 Simulation Dataset & Preprocessing

We simulate 2D pool boiling with a resolution of 256×256 lattice units (lu) using a hybrid LB-FD simulation. For simplicity, we adopt common simulation conditions (see Supplemental Information 1) which has shown to be stable [38]. Thermal simulation conditions include Dirichlet boundary conditions in the bottommost solid layer for temperature, and uniform initial bulk liquid temperature at a saturation temperature of $T_{\text{sat}} = 0.9T_c = 0.0656$ in lattice temperature unit (tu). A total of 9 sets of simulation data is generated with varying heater temperature and configurations for a diverse training dataset. Each set contains 200 frames. All heaters have a length of 40 lu and are arranged 40 lu apart from each other if there are multiple as shown in Fig. 2(b). Table 1 records the variation in heater count and heater temperature among different sets.

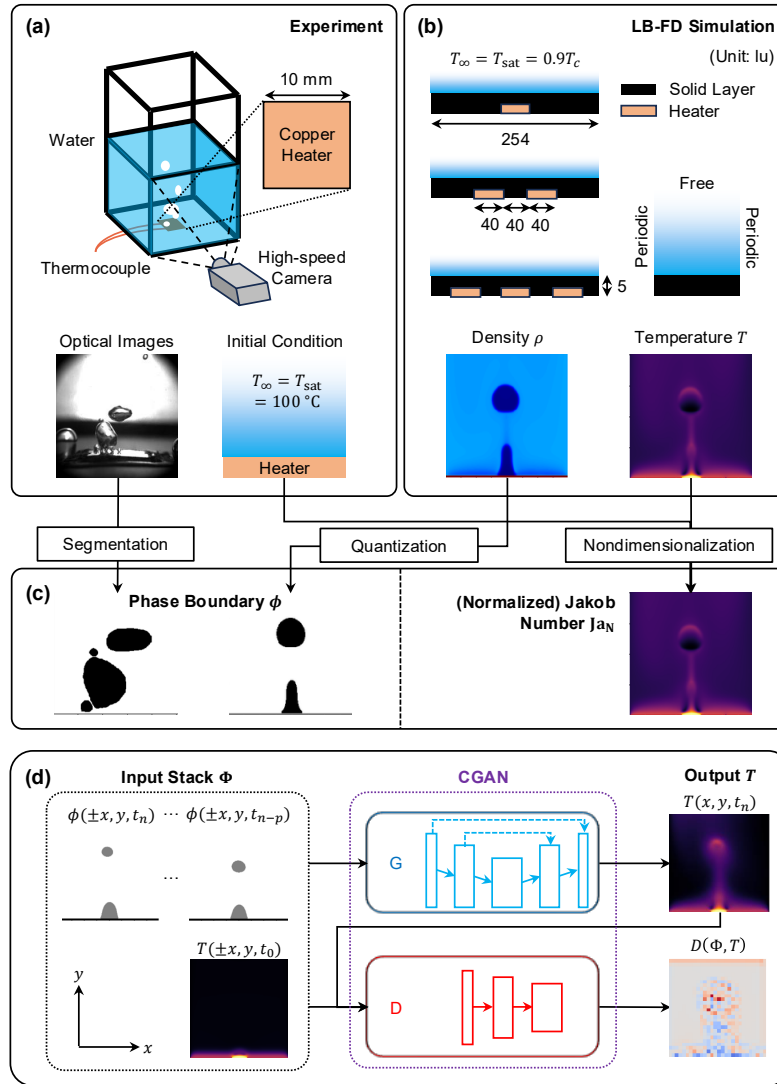


Fig. 2. Proposed framework for generating temperature data from experimental pool boiling data. (a) Experimental setup and types of data collected. (b) Simulation conditions and types of data collected. (c) The shared input format after data preprocessing. (d) Input and output groups for model training and evaluation and CGAN structure. n denotes the current frame number, and p denotes the number of previous phase contour frames included in the input group. Data augmentation, specifically horizontal mirroring, is achieved by incorporating an input stack in the form $\Phi(-x)$ in place of $\Phi(x)$.

To obtain phase contour maps ϕ from simulation, we quantize the density map ρ using a global threshold ρ_{th} derived from density distribution (see Supplemental Information 1), and manually assign values to each corresponding phase based on the following formula:

$$\phi(x, y, t) = \begin{cases} 0, & \text{if } \rho \leq \rho_{th} \text{ (vapor)} \\ 1, & \text{if } \rho > \rho_{th} \text{ (liquid)} \\ -1, & \text{for solid} \end{cases} \quad (1)$$

To normalized temperature values, we convert all temperature maps T to a normalized Jakob number Ja_N using the following equation:

$$Ja_N = \frac{c_{p,l}(T - T_{sat})}{h_{fg}} \frac{1}{Ja_{max}} = \frac{Ja}{Ja_{max}} \quad (2)$$

where c_p is the heat capacity of liquid water, h_{fg} is the latent heat of evaporation. All fluid properties are taken at saturation temperature, and the maximum Jakob number Ja_{max} is taken to be 0.222 from Table 1.

Table 1

Heater conditions used in each simulation dataset.

Dataset	Heater Count	T_{heater} (tu)	T_{heater} (K)	Ja_{heater}
1	1	0.074	656.94	0.150
2		0.076	674.69	0.186
3		0.078	692.45	0.222
4	2	0.074	656.94	0.150
5		0.076	674.69	0.186
6		0.078	692.45	0.222
7	3	0.074	656.94	0.150
8		0.076	674.69	0.186
9		0.078	692.45	0.222

3.2 Experimental Dataset & Preprocessing

We conduct pool boiling experiments and record 3 sets of high-speed images of the bubble phenomenon at different heater output, ranging from 30 W to 70 W. Each set of high-speed image sequence consists of 500 images with a resolution of 1024 x 1024 pixels at 2000 frames per second (fps). Thermocouple measurements are also taken at the heater surface, as shown in Fig. 2(a).

To obtain the phase contour maps from high-speed images, we perform instance segmentation through a pre-trained Mask R-CNN model [23]. Outputs are in the form of instance-specific masks over bubbles, isolating vapor region from the surrounding liquid region. Values within each phase region are then assigned according to Eq. (1). Solid heater layer position is estimated from the original image and manually added after segmentation (see Supplemental Information 2). We manually construct the initial temperature map by estimating the heater temperature through thermocouple measurements under the assumptions that the heater temperature remains uniform, and the bulk liquid temperature is initially at a saturation temperature $T_{sat} = 100$ °C. The initial temperature map is then normalized by Eq. (2).

Table 2

Heater condition used in each experimental dataset.

Dataset	Heater Length (mm)	Heater Power (W)	Measured Heat Flux q''_{ST} (W/cm ²)	T_{heater} (K)	Ja_{heater}
1	10	30	5.24	385.89	0.0238
2		50	14.33	388.88	0.0294
3		70	22.92	390.90	0.0332

3.3 Model Structure & Training

We define our CGAN architecture using a U-net-like generator [31,41] and a simple feedforward discriminator, as illustrated in Fig. 2(d). The generator learns an explicit mapping from input maps to the corresponding temperature field, while the discriminator implicitly learns the joint structure of the inputs and outputs by analyzing both phase contour and temperature maps together. This adversarial setup encourages the generator to produce temperature fields that are not only numerically accurate but also physically consistent with realistic phase dynamics. The training objective (see Supplemental Information 3) of the generator L_G is a weighted combination of three loss components: reconstruction loss L_{REC} , which minimizes pixel-wise differences between predicted and ground truth temperatures; boundary condition loss L_{IBC} , which enforces agreement with the initial temperature distribution at the bottommost solid layer where Dirichlet boundary condition is applied, and an adversarial loss L_{GAN} , which represents the dissimilarity between the generated images and the real images as recognized by the discriminator:

$$L_G = \lambda_{REC} L_{REC} + \lambda_{IBC} L_{IBC} + L_{GAN} \quad (3)$$

where λ_{REC} and λ_{IBC} are the weights assigned to the respective loss components. Here, we employ mean square error for both reconstruction loss and boundary loss, and binary cross-entropy for the adversarial loss. The training objective of the discriminator is to maximize the adversarial loss and conditional loss L_C which represents its inability to label real images as real:

$$L_D = -L_{GAN} + L_C \quad (4)$$

To improve model robustness and generalization, as well as to compensate for the lack of imposable physical constraints, we investigate the effect of enforcing perspective invariance. This is implemented either as a data augmentation technique—by horizontally mirroring the input contour maps during training—or as an additional loss computation, where the total losses for both the original and mirrored inputs are summed. This strategy encourages the model to produce consistent inference regardless of viewing orientation.

To evaluate the model’s ability to generalize across varying heater conditions, we train on simulation datasets 1, 3, 4, and 6, which collectively span the full range of heater temperatures and include two distinct heater geometries. As shown in Fig. 2(d), each input stack includes a set of phase contour maps and a normalized initial temperature map. For the results presented in this work, we use an input configuration with $p = 2$ (unless specified otherwise), meaning that each input stack includes two additional phase contour maps from the preceding time steps to provide temporal context. Table 3 summarizes all model configurations used in the subsequent analysis.

Table 3

Model variations used for the subsequent analysis.

Model Number	Weight ($\lambda_{REC}, \lambda_{IBC}$)	Augmentation Type
1 (Baseline CGAN)	(10,0)	None
2	(10,5)	None
3	(10,5)	Input Augmentation
4	(10,5)	Additional Loss

4. Results & Discussion

4.1 Model Performance Evaluation with Simulation Data

To evaluate the performance of our model across a range of boiling conditions, we conduct a comprehensive analysis using simulation datasets. This includes assessing its ability to reproduce global heat flux trends, capture transient temporal behavior, and maintain accuracy across different phase regions. We further analyze how the model performs during distinct boiling regimes and examine the spatial and temporal distribution of prediction errors. Together, these evaluations provide a multi-scale perspective on model accuracy and offer insight into the physical interpretability of the predictions.

We begin by evaluating whether each model reproduces expected trends in spatiotemporally averaged surface heat flux q''_{ST} across datasets. We first approximate the local surface heat flux $q''(x, y_h, t)$ at the heater surface $y = y_h$ using the following equation:

$$q''(x, y_h, t) = -\kappa(x, y_h + \Delta y, t) \frac{\Delta T}{\Delta y} \quad (5)$$

where $\kappa(x, y_h + \Delta y, t)$ is the thermal conductivity of the fluid cell adjacent to the solid cell at location (x, y_h) , $\Delta T = T(x, y_h + \Delta y, t) - T(x, y_h, t)$ is the temperature difference between the top solid cell and the adjacent fluid cell, and Δy is the discretized distance, which is equal to the pixel size. The spatially averaged surface heat flux q''_S is:

$$q''_S(t) = \frac{1}{L_x} \sum_{x=1}^{L_x} q''(x, y_h, t) \quad (6)$$

and the spatiotemporally average surface heat flux q''_{ST} of one dataset is then:

$$q''_{ST} = \frac{1}{N} \sum_{t=0}^N q''_S(t) \quad (7)$$

where $L_x = 254$ lu is the length of the solid layer, and N is the number of frames in that dataset.

All values are first converted back to physical units using the principle of corresponding states [42] (see Supplemental Information 1). Fig. 3(a) shows the inferred and ground truth values of q''_{ST} across all simulation datasets. Among all models evaluated, only model 4 captures the expected physical trend of increasing surface heat flux with higher heater temperatures and decreasing flux as the number of heater elements increases. Other models exhibit partial trends, for example model 3 only learns a decrease in q''_{ST} as heater temperature decreases.

Table 4

Root mean square error of the predicted heat flux values across different models.

Model	$\Delta q''_{ST}$ (W/cm ²)	$\Delta q''_S$ (W/cm ²)
1	0.375	0.395
2	0.182	0.200
3	0.171	0.181
4	0.037	0.054

Next, we examine the model's ability to capture transient behavior by comparing the temporal evolution of the spatially averaged surface heat flux $q''_S(t)$, as shown in Fig. 3(b). For this analysis, we focus on dataset 8 as an

example (see SI-4 for other evaluations). All models, except for the baseline GAN (model 1), reproduce the overall fluctuation patterns observed in the ground truth heat flux (i.e. the inferred heat flux is in-phase with the ground truth heat flux). Among them, model 4 shows the smallest deviation from the ground truth heat flux across all time steps. To concretely evaluate the prediction accuracy of each model, we compute the root mean square error (RMSE) values between the inferred and ground truth q''_{ST} and q''_S , which are summarized in Table 4. Model 4 has the lowest RMSE values on all metrics.

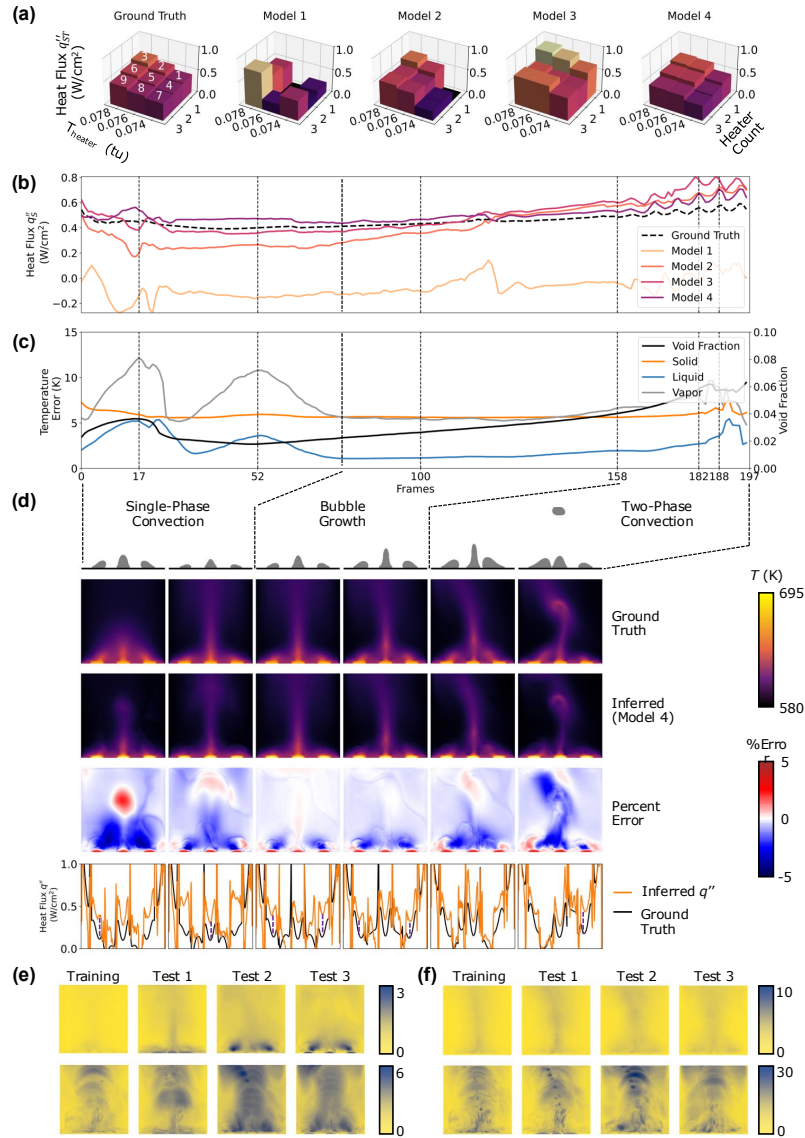


Fig. 3. Model evaluation on simulation datasets. (a) Ground truth and inferred q''_{ST} . Dataset number is labelled on the ground truth plot. (b) Ground truth and inferred q''_S over time for dataset 8. (c) Inference error in different phase regions over time for dataset 8 with model 4. (d) Snapshots of the inference results. Each column matches the labelled frame number (17, 52, 100, 158, 182, 188) on (b) and (c). Purple dashed lines across the heat flux graph show rough consistent offsets between ground truth and prediction. (e) Average (top row) and maximum (bottom row) percent error in temperature inference from model 4 over all frames of different test groups. (f) Average (top row) and maximum (bottom row) error in successive temperature difference (unit: K) from model 4 over all frames of different test groups.

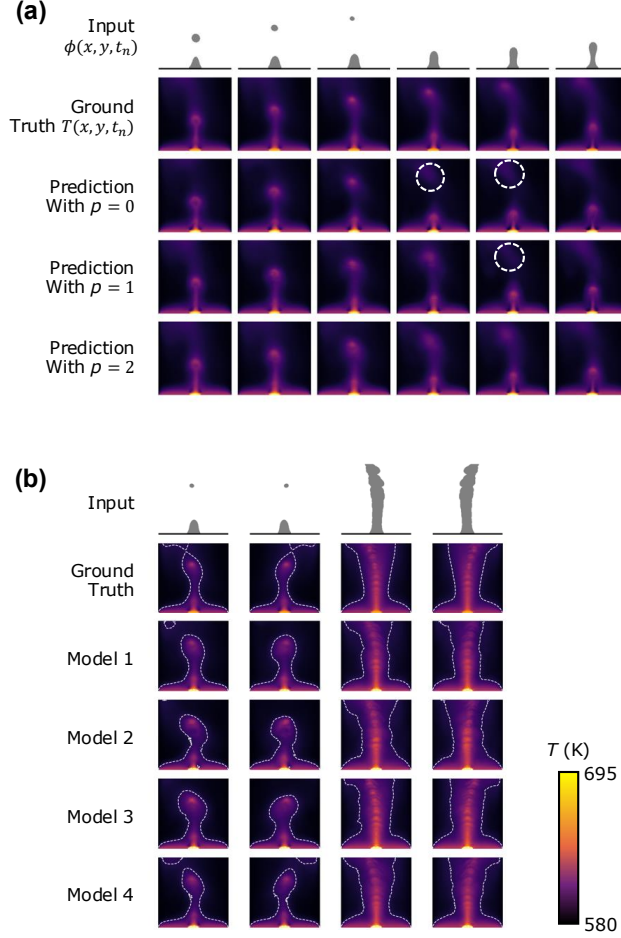


Fig. 4. Effect of (a) input group and (b) data augmentation on model inference accuracy for simulation datasets. White dashed contour lines encircle regions with a temperature higher than 595 K. The last two columns of (b) show the vapor trajectory and the maximum temperature reached across all frames.

Since surface heat flux calculation involves quantities in all three phases, it is crucial to measure inference accuracy for each phase region to identify the main sources of error. Using model 4 and dataset 8, Fig. 3(c) shows the spatially averaged error within each phase region over time. We in addition plot void fraction f over time, which is calculated as follows:

$$f = \frac{A_g}{A_l + A_g} = \frac{A_g}{A - A_s} \quad (8)$$

where A_g, A_l, A_s, A are the vapor area, liquid area, solid area, and the entire region of interest, respectively. The void fraction of vapor serves as an indicator of the change in bubble phenomena, from which we divide each simulation dataset into three regimes: single-phase convection, bubble growth, and two-phase convection (i.e. bubble begins to depart). Representative snapshots within each regime are shown in Fig. 3(d). For a complete assessment of the model's ability to generalize under different types of condition, we also plot the spatial distributions of both average and maximum percent error in temperature T and successive temperature difference ΔT across all frames for several test cases using model 4 (Figs. 3(e) and 3(f)). We define three test cases: Test 1 includes datasets 2 and 5, where the heater temperature (0.076 tu) lies between the temperature values seen in the training set, while the heater count remains the same. Test 2 includes datasets 7 and 9, which differ from the training datasets in heater count but share the same heater temperature. Test 3 includes dataset 8, which differs from the training datasets in both heater temperature and heater count.

Solid region, despite the enforcement of initial boundary condition, exhibits a significant amount of overestimation of around 2-3% (corresponds to an error of 12-20 K) at the heaters, as shown in Fig. 3(d). We also observe this concentrated error at the heaters in both average and maximum error heatmaps from Test 3 column (Fig. 3(e)). However, the error in ΔT at the heaters for Test 3 is close to 0 (Fig. 3(f)). This implies a temporally consistent error in temperature inference at the heaters. Similar error distribution is observed in Test 1, where the temperature of the heater is different from the training datasets, but not observed in Test 2, where only the heater count is varied. This implies the imposed initial boundary condition does not greatly improve the model’s ability to interpolate between temperature but the ability to generalize across different heater configurations within the solid region. Furthermore, this consistent overestimation contributes to the overprediction in surface heat flux, indicated by the relatively constant offsets at multiple locations in Fig. 3(d). However, this does not greatly impact the qualitative interpretation of the heat flux fluctuation, namely the heat flux drop during bubble nucleation, coalescence and departure is still observed.

Vapor region contributes to the highest average and maximum error across all test cases, indicated by the darker color along the vapor flow path shown in Figs. 3(e) and 3(f) whereas liquid region has the lowest average and maximum error. Similar observations can be noted from Fig. 3(c). This is expected since vapor regions evolve more dynamically, while liquid region constitutes most of the background that remains relatively unchanged. However, occasional error peaks can be observed in both the vapor region and the liquid region shown in Figs. 3(c) and 3(d), particularly in the single-phase convection regime. This is because here the phase contour maps do not provide meaningful information on temperature distribution beyond the defined contour. Since during this regime, the vapor contour near the surface remains relatively stable while thermal energy propagates upwards through liquid only, the model is unable to fully capture thermal convection within liquid phase simply from the unchanging phase contours. Instead, the model infers thermal convection from the temperature distribution within the most stable bubble growth regime, where most of our training data lies, as seen from the similarities among the inferred temperature maps in both single-phase convection and bubble growth regimes. This additionally results in poor inference within the vapor region, as the temperature distribution within the vapor region from the bubble growth regime is also carried over (Fig. 3(d)).

This underdetermined nature of our current objective reveals the inherent deficiency in predicting physical variables (i.e. temperature) from geometric variables (i.e. phase contour) to a high degree of spatial and temporal accuracy. We further illustrate this limitation through an image sequence generated from a baseline CGAN model with varying input layers, as shown in Fig. 4(a). With $p = 0$, the process becomes a traditional image-to-image translation task, where the model generates the temperature map only from the corresponding phase contour map. However, this process shows clear loss of correlation, represented by sharp temperature discontinuity when the phase contour becomes invisible, notated by white dashed circles. This is against physical intuition that the bubble with the associated temperature variations around it should continue to propagate in time, which is observed in the ground truth temperature maps. We attempt to reduce this loss of correlation by using sequential maps containing phase contour maps from previous time steps to train the model. However, the loss of correlation persists to varying degree with $p = 1$ and $p = 2$, which is also observed from localized maximum error peaks (i.e. dark spots) scattered along the vapor flow paths in Figs. 3(e) and 3(f). Alternatively, we attempt to mitigate loss of correlation through conventional data augmentation methods. Fig. 4(b) shows the comparison between prediction with and without data augmentation. We observe that although temperature inference is accurately achieved around the vicinity of vapor region without data augmentation (i.e. model 1 and 2), loss of correlation occurs at region far away from vapor region where the model struggles to extract useful information from the contours alone. With data augmentation however (i.e. model 3 and 4), the model learns the propagation direction from imposed symmetry which helps restore inference distant from the vapor region.

4.2 Evaluation on Experimental Data

Without ground truth temperature to compare, here we rely on experimentally measured surface heat flux to analyze the model inference accuracy. Fig. 5(a) shows both the measured ground truth and the inferred spatiotemporally averaged surface heat flux q''_{ST} with different experimental datasets. Model 4 again shows the closest agreement with the measured heat flux.

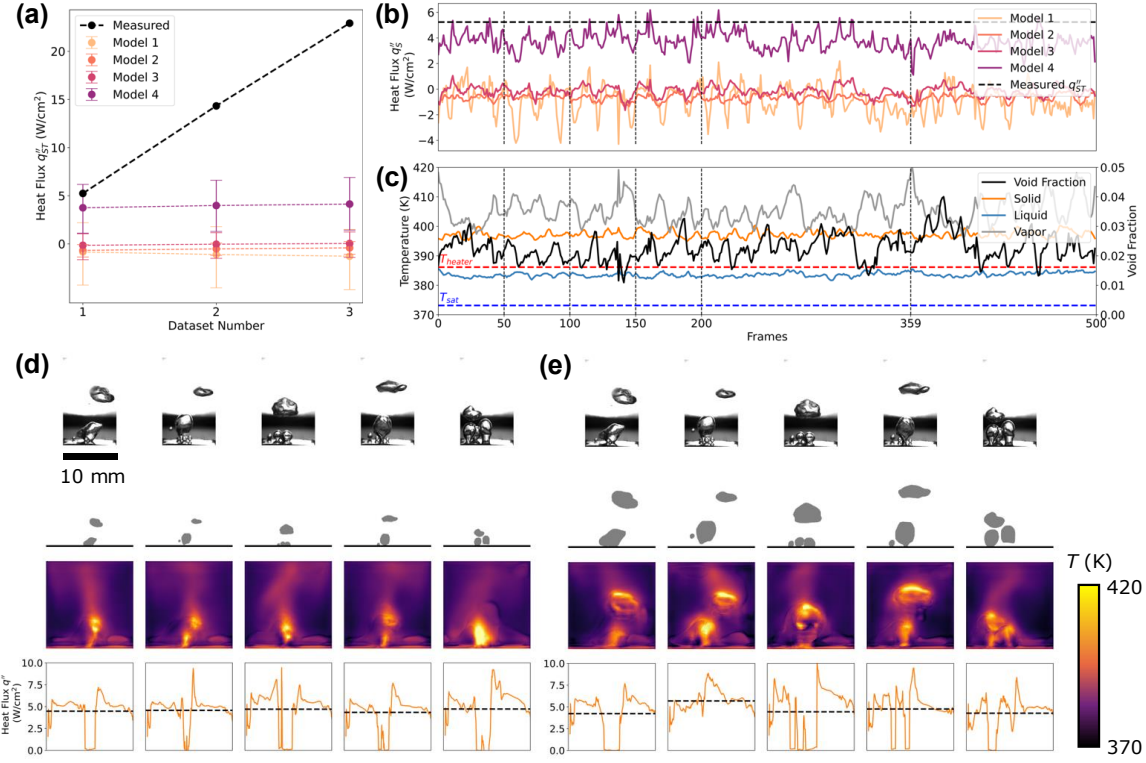


Fig. 5. Model performance on experimental datasets. (a) Measured and inferred q''_{ST} over different experimental datasets. Error bar limits show the minimum and maximum q''_S . (b) Ground truth and inferred q''_S over time for experimental dataset 1. (c) Spatially averaged temperature in different phase regions over time for experimental dataset 1 inferred by model 4. The saturation temperature and the heater temperature are labelled. (d) Inference result on experimental dataset 1 with inputs scaled equal to the simulation data. Top row is the raw image cropped to the region of interest. Each frame corresponds to each labelled frame in (b) and (c) (50, 100, 150, 200, 359). (e) Inference result with the same input frames from (d) upscaled by a factor of 2.

Fig. 5(b) shows the distribution of spatially averaged surface heat flux q''_S . Although the ground truth distribution of q''_S is also not available, we can infer from experimental measurement that q''_S is relatively uniform across time because of the constant heat output. This implies that the ground truth distribution of q''_S should have a low variance. Similar behavior is also observed in the two-phase convection regime from Fig. 3(b), where q''_S fluctuates about a stable average. This correlates with a relatively stable void fraction fluctuation, as shown in Figs. 3(c) and 5(c). Fig. 5(c) also shows that the spatially averaged temperature within each phase exhibits stable fluctuation. However, the temperature range shown is not physical, since liquid temperature is now on average higher than the saturation temperature, and vapor temperature is consistently higher than solid temperature on average. This error is due to large temperature (Jakob number) range the model needs to extrapolate. For experimental datasets, the normalized Jakob number is roughly a tenth of the simulation datasets (Table 1 and Table 2). Instead of learning temperature from the initial temperature map, the model outputs values close to those in simulation data. This difference in inference results in an overestimation of temperature in the range of 0.4-0.5 in normalized Jakob value, which corresponds to an error of 10-20 K.

Several snapshots of the inferred temperature maps for experimental dataset 1 for the are shown in Fig. 5(d). We observe that the model displays the same qualitative features found in simulation inferences, including the sharp decrease in surface heat flux during bubble growth and departure. However, given the scale of the simulation dataset, the experimental data will have a void fraction one fourth that of the simulation data. This makes temperature inference difficult within the vapor region due to its small size. Fig. 5(e) shows the inference result with

an upscaled input. We observe clearer bubble contours and temperature distribution within the bubbles, where high-temperature region is concentrated around the outer edge with a low-temperature interior, similar to that observed in simulation data.

4.3 Discussion

We have proposed and developed the specific framework for generating temperature maps from high-speed images and pointwise temperature measurement through data-driven deep learning in the context of pool boiling. This framework provides a simple alternative method to generating data without involving data such as velocity maps that are difficult to collect experimentally at a high spatial and temporal resolution. We in addition have evaluated the effectiveness of several techniques in addressing unique difficulties that arise from our use case. Specifically, to minimize the loss of correlation due to the absence of phase contour as a result of quantization or segmentation error, we implement a many-to-one image-to-image inference scheme instead of the traditional one-to-one translation, which also greatly enhances temporally consistency. Furthermore, we employ conventional data augmentation to compensate for the lack of shared physical constraints for both simulation and experiments, which improves heat flux prediction by at least 4 times (Table 4). Finally, foreseeing the mismatch between simulation and experimental datasets, we test the limit of the model by incorporating simulation and experimental data that greatly differ in thermodynamic conditions and boiling regimes. Our current implementation is still able to achieve an inference error below 6% across all simulation datasets, and a close agreement in spatiotemporally averaged heat flux value with the experimental datasets despite these difficulties. Errors mainly arise from persistent loss of correlation and large difference between simulation data and experimental data, such as differences in fluid properties (saturation temperature), heater arrangement, spatial and temporal steps, initial and boundary conditions, boiling regimes and bubble behaviors.

In summary, we have shown that even with limited training data, no strict enforcement of physics and no dedicated model optimization, the model is capable of making qualitatively accurate inferences on relevant thermodynamic variables including temperature distribution within each phase region and surface heat flux. This demonstrates the immense potential of our proposed data-driven framework, and the possibility for future quantitative analysis with more diverse training datasets and better model architecture. Moreover, our methods can be extended to other multiphase systems where image data can be readily obtained, owing to its simplistic and general formulation.

Acknowledgements

Q.F. is thankful for the financial support from the UC Irvine Mechanical and Aerospace Engineering Department for graduate student researcher. The authors gratefully acknowledge funding support from the Office of Naval Research (ONR) MURI under Grant No. N000142412575 with Dr. Mark Spector serving as the program officer, and funding support from the National Science Foundation (NSF) under Grant No. 2045322.

CRedit Authorship Contribution Statement

Qianxi Fu: Methodology, Software, Formal Analysis, Writing – Original Draft, Writing – Review & Editing, Visualization. **Youngjoon Suh:** Conceptualization, Methodology, Software, Investigation, Writing – Review & Editing, Supervision. **Xiaojing Zhang:** Investigation, Data curation. **Yoonjin Won:** Conceptualization, Writing – Review & Editing, Supervision, Project Administration, Funding Acquisition.

Conflict of Interests

There are no conflicts to declare.

References

- [1] J. Dirker, D. Juggurnath, A. Kaya, E.A. Osowade, M. Simpson, S. Lecompte, S.M.A. Noori Rahim Abadi, V. Voulgaropoulos, A.O. Adelaja, M.Z. Dauhoo, et al. Thermal energy processes in direct steam generation solar systems: Boiling, condensation and energy storage – A Review, *Front. Energy Res.* 147 (6) (2019). <https://doi.org/10.3389/fenrg.2018.00147>

- [2] S. Fan, F. Duan. A review of two-phase submerged boiling in thermal management of electronic cooling. *Int. J. Heat Mass Transf.* 150 (2020) 119324. <https://doi.org/10.1016/j.ijheatmasstransfer.2020.119324>
- [3] D.B.R. Kenning. Optical studies of boiling heat transfer: insights and limitations. *Int. J. Heat Fluid Flow, Selected Papers from the 5th ECI International Conference on Boiling Heat Transfer* 25 (2004) 209–222. <https://doi.org/10.1016/j.ijheatfluidflow.2003.11.010>
- [4] J. Kim, Review of nucleate pool boiling bubble heat transfer mechanisms. *Int. J. Multiph. Flow* 35 (2009) 1067–1076. <https://doi.org/10.1016/j.ijmultiphaseflow.2009.07.008>
- [5] R.F. Gaertner, Photographic Study of Nucleate Pool Boiling on a Horizontal Surface. *ASME. J. Heat Transfer.* 87 (1965) 17–27. <https://doi.org/10.1115/1.3689038>
- [6] M. Bongarala, J.A. Weibel, S.V. Garimella, A method to partition boiling heat transfer mechanisms using synchronous through-substrate high-speed visual and infrared measurements. *Int. J. Heat Mass Transf.* 226 (2024) 125516. <https://doi.org/10.1016/j.ijheatmasstransfer.2024.125516>
- [7] M.V. Piskunov, P.A. Strizhak, Using Planar Laser Induced Fluorescence to explain the mechanism of heterogeneous water droplet boiling and explosive breakup. *Exp. Therm. Fluid Sci.* 91 (2018) 103–116. <https://doi.org/10.1016/j.expthermflusci.2017.10.018>
- [8] Y. Suh, C.-H., Lin, H. Gowda, Y. Won, Multiscale Evaporation Rate Measurement Using Microlaser-Induced Fluorescence. *J. Electron. Packag.* 142 (2020). <https://doi.org/10.1115/1.4046767>
- [9] D. Schubring, A.C. Ashwood, T.A. Shedd, E.T. Hurlburt, Planar laser-induced fluorescence (PLIF) measurements of liquid film thickness in annular flow. Part I: Methods and data. *Int. J. Multiph. Flow* 36 (2010) 815–824. <https://doi.org/10.1016/j.ijmultiphaseflow.2010.05.007>
- [10] S. Sahu, Y. Hardalupas, A.M.K.P Taylor, Simultaneous droplet and vapour-phase measurements in an evaporative spray by combined ILIDS and PLIF techniques. *Exp. Fluids* 55 (2014) 1673. <https://doi.org/10.1007/s00348-014-1673-0>
- [11] C.R. Kharangate, I. Mudawar, Review of computational studies on boiling and condensation. *Int. J. Heat Mass Transf.* 108 (2017) 1164–1196. <https://doi.org/10.1016/j.ijheatmasstransfer.2016.12.065>
- [12] S. M. S. Hassan, et al, BubbleML: A multiphase multiphysics dataset and benchmarks for machine learning. *Adv. Neural Inf. Process. Syst.* 36 (2023) 418–449.
- [13] G. Son, V.K. Dhir, N. Ramanujapu, Dynamics and Heat Transfer Associated With a Single Bubble During Nucleate Boiling on a Horizontal Surface. *ASME. J. Heat Transfer.* 121 (3) (1999) 623–631. <https://doi.org/10.1115/1.2826025>
- [14] G. Son, V.K. Dhir, Numerical simulation of nucleate boiling on a horizontal surface at high heat fluxes. *Int. J. Heat Mass Transf.* 51 (2008) 2566–2582. <https://doi.org/10.1016/j.ijheatmasstransfer.2007.07.046>
- [15] A.C. Pattnaik, R. Samanta, H. Chattopadhyay, A brief on the application of multiphase lattice Boltzmann method for boiling and evaporation. *J. Therm. Anal. Calorim.* 148, (2023) 2869–2904. <https://doi.org/10.1007/s10973-022-11820-8>
- [16] H. Jiang, Y. Liu, H. Chu, A review of numerical investigation on pool boiling. *J. Therm. Anal. Calorim.* 148 (2023) 8697–8745. <https://doi.org/10.1007/s10973-023-12292-0>
- [17] Y. Suh, A. Chandramowlishwaran, Y. Won, Recent progress of artificial intelligence for liquid-vapor phase change heat transfer. *NPJ. Comput. Mater.* 10 (2024) 65. <https://doi.org/10.1038/s41524-024-01223-8>

- [18] S. Chang, et al, BubbleMask: Autonomous visualization of digital flow bubbles for predicting critical heat flux. *Int. J. Heat Mass Transf.* 217 (2023) 124656. <https://doi.org/10.1016/j.ijheatmasstransfer.2023.124656>
- [19] J. Lee, et al, Computer vision-assisted investigation of boiling heat transfer on segmented nanowires with vertical wettability. *Nanoscale* 14.36 (2022) 13078-13089. <https://doi.org/10.1039/D2NR02447K>
- [20] C. Zhao, Y. Suh, Y. Won, DropletMask: Leveraging visual data for droplet impact analysis. *Droplet* 3.4 (2024) e137. <https://doi.org/10.1002/dro2.137>
- [21] S. Khodakarami, et al, Machine learning enabled condensation heat transfer measurement. *Int. J. Heat Mass Transf.* 194 (2022) 123016. <https://doi.org/10.1016/j.ijheatmasstransfer.2022.123016>
- [22] Y. Suh, et al, A deep learning perspective on dropwise condensation. *Adv. Sci.* 8.22 (2021) 2101794. <https://doi.org/10.1002/advs.202101794>
- [23] Y. Suh, R. Bostanabad, Y. Won, Deep learning predicts boiling heat transfer. *Sci. Rep.* 11 (2021) 5622. <https://doi.org/10.1038/s41598-021-85150-4>
- [24] S. Torisaki, S. Miwa, Robust bubble feature extraction in gas-liquid two-phase flow using object detection technique. *J. Nucl. Sci. Technol.* 57 (2020) 1231–1244. <https://doi.org/10.1080/00223131.2020.1779145>
- [25] I. Malakhov, A. Seredkin, A. Chernyavskiy, V. Serdyukov, R. Mullyadzanov, A. Surtaev, Deep learning segmentation to analyze bubble dynamics and heat transfer during boiling at various pressures. *Int. J. Multiph. Flow* 16 (2023) 104402. <https://doi.org/10.1016/j.ijmultiphaseflow.2023.104402>
- [26] G.M. Hobold, A.K. da Silva, Visualization-based nucleate boiling heat flux quantification using machine learning. *Int. J. Heat Mass Transf.* 134 (2019) 511–520. <https://doi.org/10.1016/j.ijheatmasstransfer.2018.12.170>
- [27] M. Raissi, P. Perdikaris, G.E. Karniadakis, Physics-informed neural networks: A deep learning framework for solving forward and inverse problems involving nonlinear partial differential equations. *J. Comput. Phys.* 378 (2019) 686–707. <https://doi.org/10.1016/j.jcp.2018.10.045>
- [28] S. Cai, Z. Wang, S. Wang, P. Perdikaris, G.E. Karniadakis, Physics-Informed Neural Networks for Heat Transfer Problems. *ASME. J. Heat Transfer.* 143 (2021). <https://doi.org/10.1115/1.4050542>
- [29] S. Cai, Z. Mao, Z. Wang, M. Yin, G.E. Karniadakis, Physics-informed neural networks (PINNs) for fluid mechanics: a review. *Acta Mech. Sin.* 37 (2021) 1727–1738. <https://doi.org/10.1007/s10409-021-01148-1>
- [30] I.J. Goodfellow, J. Pouget-Abadie, M. Mirza, B. Xu, D. Warde-Farley, S. Ozair, A. Courville, Y. Bengio, Generative Adversarial Networks. (2014) <https://doi.org/10.48550/arXiv.1406.2661>
- [31] P. Isola, J.-Y. Zhu, T. Zhou, A.A. Efros, Image-to-Image Translation with Conditional Adversarial Networks. (2018) <https://doi.org/10.48550/arXiv.1611.07004>
- [32] T.-C. Wang, M.-Y. Liu, J.-Y. Zhu, A. Tao, J. Kautz, B. Catanzaro, High-Resolution Image Synthesis and Semantic Manipulation with Conditional GANs. (2018) <https://doi.org/10.48550/arXiv.1711.11585>
- [33] X. Wang, K. Yu, S. Wu, J. Gu, Y. Liu, C. Dong, C.C. Loy, Y. Qiao, X. Tang, ESRGAN: Enhanced Super-Resolution Generative Adversarial Networks. (2018) <https://doi.org/10.48550/arXiv.1809.00219>
- [34] M.Z. Yousif, L. Yu, H.-C. Lim, Super-resolution reconstruction of turbulent flow fields at various Reynolds numbers based on generative adversarial networks. *Phys. Fluids* 34 (1) (2022) 015130. <https://doi.org/10.1063/5.0074724>

- [35] L. Yu, M.Z. Yousif, Y.-W. Lee, X. Zhu, M. Zhang, P. Kolesova, H.-C. Lim, Predicting unavailable parameters from existing velocity fields of turbulent flows using a GAN-based model. *Phys. Rev. Fluids* 9 (2024) 024603. <https://doi.org/10.1103/PhysRevFluids.9.024603>
- [36] Z. Xia, Z. Cui, Y. Chen, Y. Hu, H. Wang, Generative adversarial networks for dual-modality electrical tomography in multi-phase flow measurement. *Measurement (Lond)* 173 (2021) 108608. <https://doi.org/10.1016/j.measurement.2020.108608>
- [37] D. Hu, J. Li, Y. Liu, Y. Li, Flow Adversarial Networks: Flowrate Prediction for Gas–Liquid Multiphase Flows Across Different Domains. *IEEE Trans. Neural Netw. Learn. Syst.* 31 (2020) 475–487. <https://doi.org/10.1109/TNNLS.2019.2905082>
- [38] Q. Li, Q.J. Kang, M.M. Francois, Y.L. He, K.H. Luo, Lattice Boltzmann modeling of boiling heat transfer: The boiling curve and the effects of wettability. *Int. J. Heat Mass Transf.* 85 (2015) 787–796. <https://doi.org/10.1016/j.ijheatmasstransfer.2015.01.136>
- [39] M. Mirza, S. Osindero, Conditional Generative Adversarial Nets. (2014) <https://doi.org/10.48550/arXiv.1411.1784>
- [40] K. He, G. Gkioxari, P. Dollár, R. Girshick, Mask R-CNN (2018). <https://doi.org/10.48550/arXiv.1703.06870>
- [41] O. Ronneberger, P. Fischer, T. Brox, U-Net: Convolutional Networks for Biomedical Image Segmentation, in: N. Navab, J. Hornegger, W.M. Wells, A.F. Frangi, (Eds.), *Medical Image Computing and Computer-Assisted Intervention – MICCAI 2015*. Springer International Publishing, Cham, (2015) 234–241. https://doi.org/10.1007/978-3-319-24574-4_28
- [42] P. Yuan, L. Schaefer, Equations of state in a lattice Boltzmann model. *Phys. Fluids* 18 (2006) 042101. <https://doi.org/10.1063/1.2187070>

Supplemental Information

S1. Simulation Data Generation, Characterization & Processing

S1.1 Simulation Methods

We use a hybrid scheme with pseudopotential LBM with single relaxation time (SRT) and finite difference method (FDM), similar to the setup in [1], to generate pool boiling simulation data used in this paper.

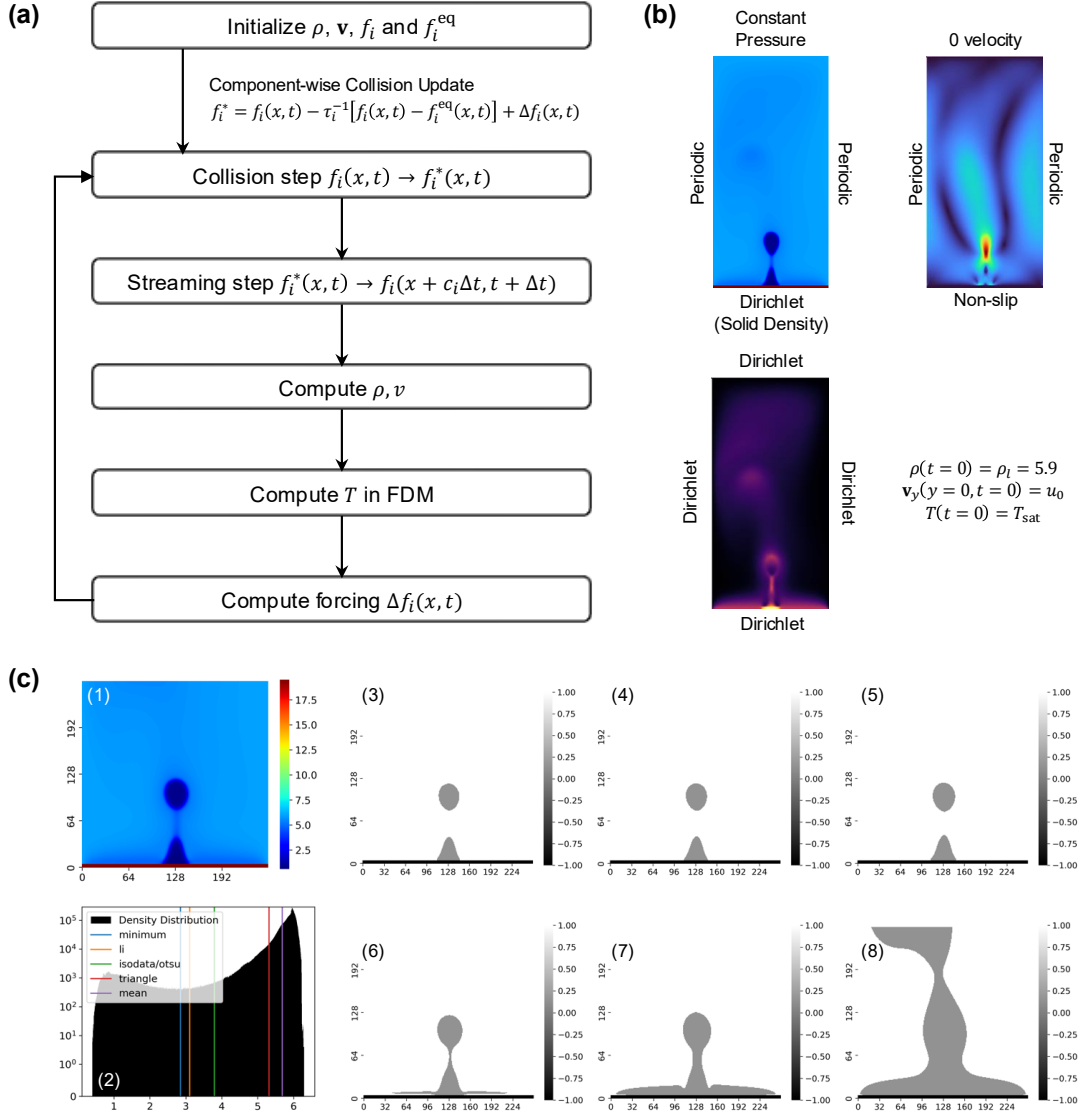


Fig. S1: LB-FD simulation data details. (a) LB-FD simulation flowchart. (b) Imposed initial and boundary conditions. The (upward) initial velocity is only applied at the solid surface, with everywhere else at 0 velocity. (c) Effects of different quantization methods. (1) original density map, (2) probability density distribution of the density values in the training datasets (dataset 1,3,4,6), (3) $\rho_{th} = 2.85$ (minimum), (4) $\rho_{th} = 3.11$ (Li), (5) $\rho_{th} = 3.80$ (ISODATA, Otsu), (6) $\rho_{th} = 4.90$, (7) $\rho_{th} = 5.31$ (triangle), (8) $\rho_{th} = 5.685$ (mean).

We conduct 2D pool boiling simulation according to the flowchart shown in Fig. S1(a) using two-dimensional lattice with nine unit lattice vectors (D2Q9). Each simulation frame has a resolution of 512 x 256 lattice units (lu). The initial and boundary conditions imposed on each variable are shown in Fig. S1(b). Note that for our objective, simulation data is cropped to 256 x 256 during pre-processing for the purpose of squaring the input and creating a free boundary at the top, reducing processing load and matching partially with the experimental data.

During simulation, the probability distribution function $f_i(x, v, t)$ along each lattice direction i is updated due to collision and streaming, from which the density ρ and velocity fields \mathbf{v} are computed. Thermal simulation is coupled with LBM through the following energy equation:

$$\frac{\partial T}{\partial t} = -\mathbf{v} \cdot \nabla T + \frac{1}{\rho c_v} \nabla \cdot (\kappa \nabla T) - \frac{T}{\rho c_v} \left(\frac{\partial P}{\partial T} \right)_\rho \nabla \cdot \mathbf{v}$$

where c_v is the heat capacity at constant volume of the liquid and κ is the thermal conductivity. The energy equation is advanced through FDM with second-order and fourth-order Runge-Kutta method applied to spatial and temporal discretization respectively. The pressure term P is related to density and temperature through the Peng-Robinson (P-R) equation of state:

$$P = \frac{\rho R T}{1 - b\rho} - \frac{a\rho^2 \varepsilon(T)}{1 + 2b\rho - b^2\rho^2}, \quad \begin{cases} a = 0.45724 R^2 T_c^2 / P_c \\ b = 0.0778 R T_c / P_c \end{cases}$$

where P_c and T_c denote the critical pressure and temperature respectively. The ideal gas constant R is taken to be 1 in LB unit, and $a = 2/49$ and $b = 2/21$ are used. The expression $\varepsilon(T)$ is given by:

$$\varepsilon(T) = [1 + (0.37464 + 1.54226\omega - 0.26992\omega^2)(1 - \sqrt{T/T_c})]^2$$

Here $\omega = 0.344$ is taken, since it has been shown that with this value the coexistence curve derived from the above equation of state matches closely with the experimental data for saturated water-steam system [?]. Finally, the forcing term is updated based on pseudopotential formulation:

$$F_{int}(x) = -\Psi(x) \sum_{x'} G(x, x') \Psi(x') (x' - x), \quad \Psi(x) = \sqrt{\frac{2(P - \rho c_s^2)}{c_0 g}}$$

All relevant constants used in the LBM simulation are listed in Table S1 in terms of both the LB unit and the corresponding physical unit. Unit conversion is based on the principle of corresponding states [2], where any value x in physical unit with its respective critical value x_c (or characteristic value with a zero subscript) follows this relationship:

$$\frac{x}{x_c} = \frac{x_{LB}}{x_{c, LB}}$$

where the LB subscript denotes values in LB units. Certain values such as heat capacity and latent heat of vaporization do not have a critical value for conversion. Their values in physical units are directly referenced from tables at saturation temperature when the calculation requires.

S1.2 Determination of Quantization Threshold

The phase contour maps are generated through density map quantization or thresholding. We derive a global threshold value ρ_{th} by applying built-in methods such as triangle and ISODATA thresholding in python to training datasets (i.e. simulation dataset 1,3,4 and 6) only. Fig. S1(c) shows the effect of different threshold values on density maps. For the results presented in the main text, we have selected the threshold of $\rho_{th} = 3.79552$ (from ISODATA or Otsu's methods) simply based on a qualitative assessment of the resulting phase contour maps (i.e. the bubble outline follows our intuitive assignment) rather than its potential impact on model training and inference.

Table S1

Relevant constants used in simulation in both LBM and physical units. The LBM lattice unit for mass, length, time and temperature are mu, lu, ts, and tu, respectively.

Simulation Constants	LBM Unit	Physical Unit
T_c	0.0729 tu	647.17 K
ρ_c	2.657304 mu/lu ³	322 kg/m ³
u_0	0.02627 lu/ts	0.1645 m/s
l_0	23.00421 lu	2.762×10 ⁻³ m
t_0	875.6753 ts	0.01679 s
g	3×10 ⁻⁵ lu/ts ²	9.81 m/s ²
σ	0.09716	74.8×10 ⁻³ N/m

S2. Experimental Data Pre-Processing

We follow the flowchart shown in Fig. S2 to extract phase contour maps from high-speed images. We first use a fine-tuned Mask R-CNN model to perform instance segmentation on high-speed recordings to isolate vapor region [3]. The Mask R-CNN model was trained specifically for pool boiling using a meticulously curated dataset of 5,555 training images and 1,388 test images. These images were collected over several years from diverse experimental setups to capture the wide-ranging complexities of pool boiling phenomena. A team of trained annotators followed detailed project-specific guidelines to ensure consistent and accurate labeling. Regular communication among annotators helped resolve ambiguities and refine annotation standards, further enhancing the quality of the dataset. The annotation process was managed using Supervisely (San Jose, CA, USA), a commercial platform designed for efficient labeling workflows and employed human-in-the-loop techniques to iteratively address edge cases and challenging scenarios. To improve the model's generalizability, the dataset was diversified by incorporating images captured under various experimental conditions, such as different heat flux levels and surface properties. Additional variability was introduced using data augmentation techniques, including horizontal flips, brightness adjustments, contrast modifications, and resizing. These augmentations effectively expanded the dataset, simulating a broader range of conditions and improving the robustness of the trained model. The Mask R-CNN model was trained using stochastic gradient descent with a learning rate of 0.0008, a momentum of 0.9, and over 100 epochs. These training parameters were optimized to balance convergence and stability, resulting in a model that achieved a test loss of 0.046, demonstrating high accuracy in bubble detection and segmentation.

The outputs of the trained Mask R-CNN model are 8-bit instance-specific masks, with each bubble instance assigned a unique intensity value ranging from 1 to 256, representing its unique ID. Image masks then are cropped to heater (bubble-surface contact line) and only the bubble masks generated from the heater are kept. Images are then cropped and resized to a resolution of 256 x 256 with the same quantized values assigned to each phase region. The required dimension X such that the size of each pixel in the experimental datasets match that in the simulation datasets in physical units after resizing is:

$$X = \frac{256(\Delta x_{LB})}{\Delta x} = \frac{256\left(\frac{l_0}{l_{0,LB}}\right)}{\left(\frac{L_{heater}}{L_{heater,PX}}\right)}$$

where l_0 is the characteristic length of the simulation (Table S1), and $L_{heater} = 10$ mm is the length of the heater with an original pixel length of $L_{heater,PX} = 520$ pixels. In our case, matching the pixel size may require a resolution X greater than 1024. We instead pad the image to 2048 x 2048 with liquid cells at saturation temperature after

cropping so that sufficient pixels are available for resizing. The solid layer is added after resizing with a thickness of 5 pixels and spanning the full length of 256 pixels.

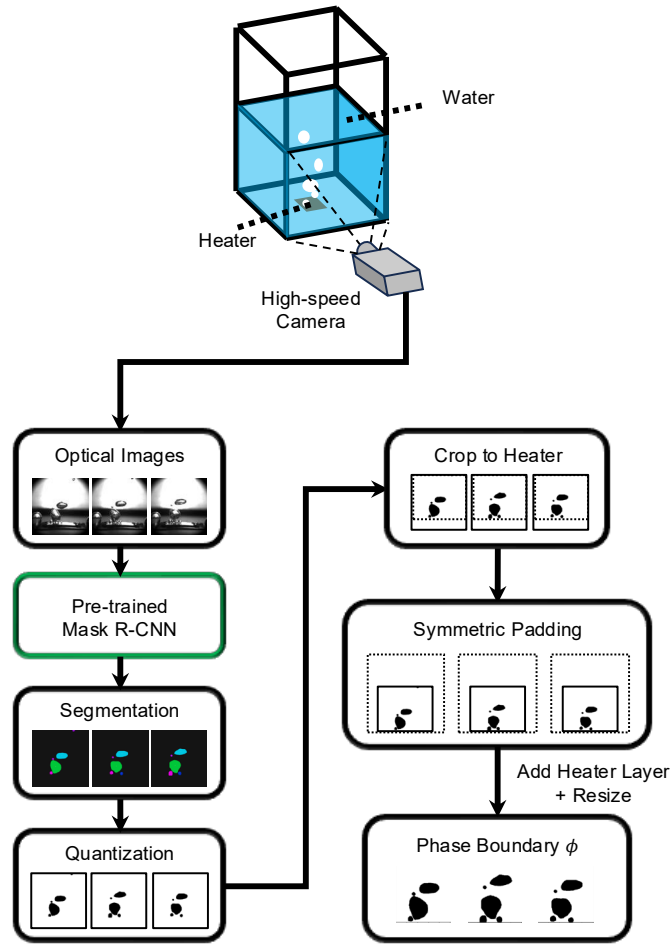


Fig. S2: Experimental data pre-processing steps. (a) Phase contour extraction. (b) Thermocouple arrangement and heating variations.

S3. Model Training Details

S3.1 CGAN Structure & Selected Parameters

Figs. S3(a) and S3(b) show the structure of the generator and the discriminator, respectively. Each 2D convolution layer in the generator has a kernel size of 5×5 , with batch normalization applied, leaky ReLU activation (except the last layer with a hyperbolic tangent activation), paddings to preserve dimension and no bias term. The 2D convolution layers in the discriminator follow similar implementation, except the kernel sizes are 7×7 , 5×5 , 3×3 , 5×5 for each layer, respectively. The initializer in both the generator and the discriminator is a random initializer sampled from a normal distribution with mean of 0 and a standard deviation of 0.01, except the last layer in both which uses a He normal initializer. We use up-sampling layer followed by a stride-1 2D convolution to avoid checkerboard artifacts that result from 2D transposed convolution [4].

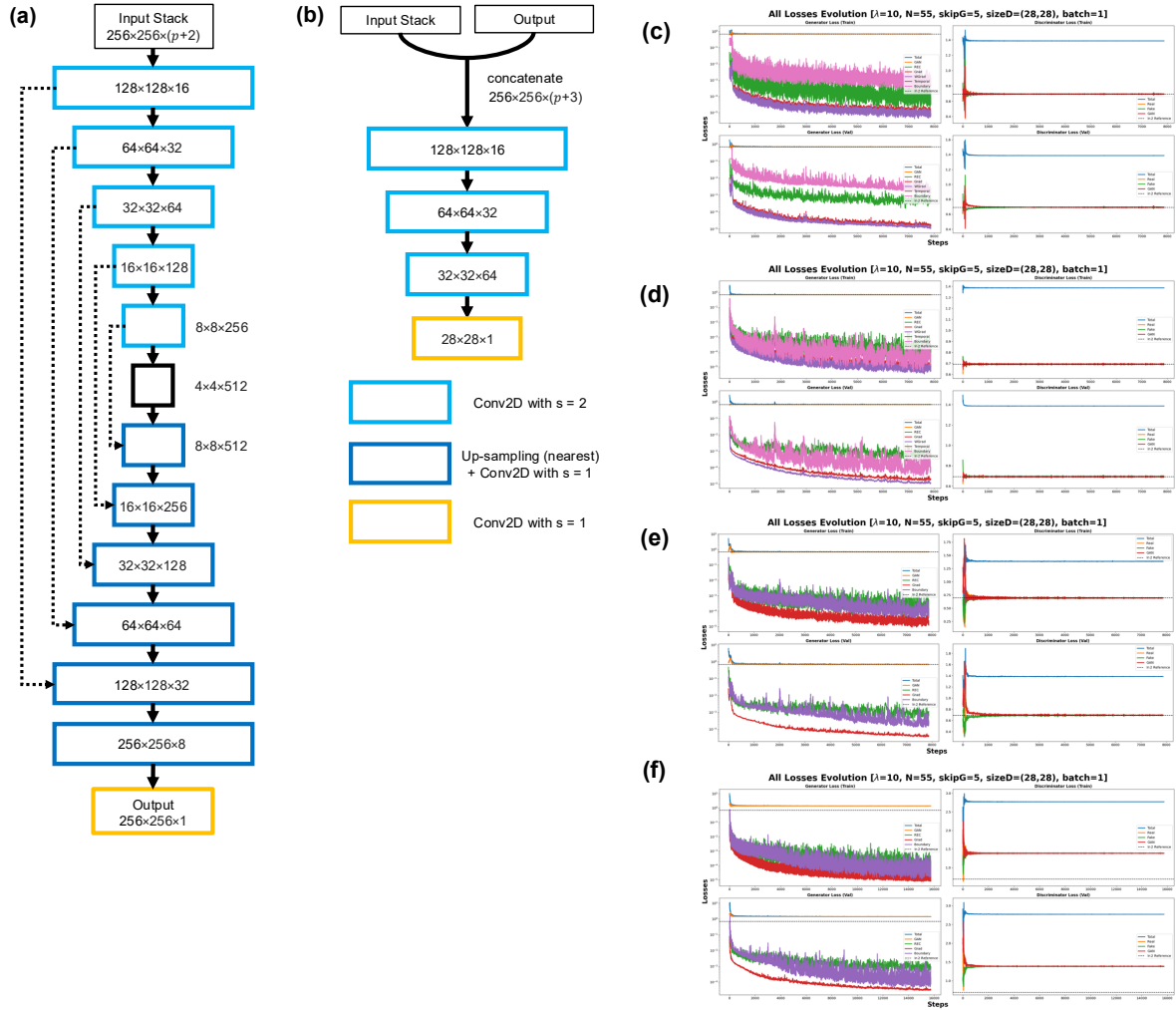


Fig. S3: Model training details. (a) Generator structure. (b) Discriminator structure. Training losses evolution of (c) model 1, (d) model 2, (e) model 3, (f) model 4.

S3.2 Training Losses

Each model is trained with a batch size of 1. We use Adam optimizer [5] with a learning rate of 0.0001 and default momentum parameters of $(\beta_1, \beta_2) = (0.9, 0.999)$. The training losses over 10 epochs (7870 steps) for each model (1 through 4) is shown in Figs. S3(c-f). The adversarial losses should fluctuate about $\ln 2$ to ensure continuous

learning. During training, we find the discriminator usually learns faster than the generator, as a result we train the generator three times at each step instead of one.

S4. Additional Data & Results

S4.1 Inference Results on Simulation Data

Figs. S4(a) and S4(b) show the spatial error distribution in both temperature and successive temperature difference on all data groups mentioned in Section 4.1.

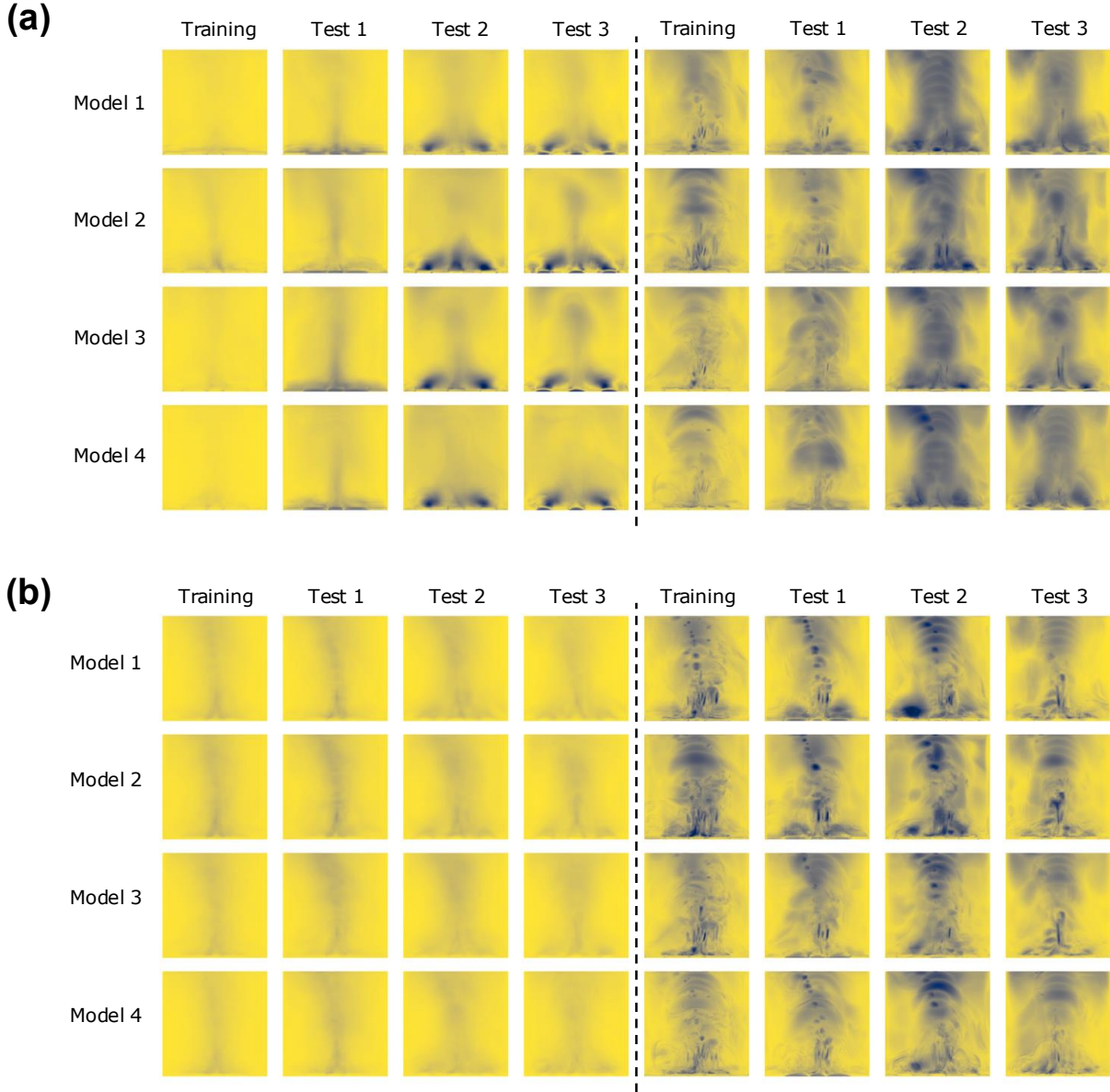


Fig. S4: Spatial distribution of (a) percent error in temperature and (b) error in successive temperature difference in Kelvin. Average errors are shown in the first 4 columns, maximum errors are shown in the last 4 columns. Corresponding scale bar is the same as shown in Fig. 3.

References (Supplemental)

- [1] Q. Li, Q.J. Kang, M.M. Francois, Y.L. He, K.H. Luo, Lattice Boltzmann modeling of boiling heat transfer: The boiling curve and the effects of wettability. *Int. J. Heat Mass Transf.* 85 (2015) 787–796.
<https://doi.org/10.1016/j.ijheatmasstransfer.2015.01.136>
- [2] P. Yuan, L. Schaefer, Equations of state in a lattice Boltzmann model. *Phys. Fluids* 18 (2006) 042101.
<https://doi.org/10.1063/1.2187070>
- [3] Y. Suh, R. Bostanabad, Y. Won, Deep learning predicts boiling heat transfer. *Sci. Rep.* 11 (2021) 5622.
<https://doi.org/10.1038/s41598-021-85150-4>
- [4] A. Odena, V. Dumolin, C. Olah, Deconvolution and Checkerboard Artifacts, *Distill* (2016)
<http://doi.org/10.23915/distill.00003>
- [5] D.P. Kingma, J. Ba, Adam: A Method for Stochastic Optimization. (2017)
<https://doi.org/10.48550/arXiv.1412.6980>